

Dojo: A Differentiable Physics Engine for Robotics

Taylor A. Howell^{1*}, Simon Le Cleac’h^{1*}, Jan Brüdigam², J. Zico Kolter³, Mac Schwager⁴,
and Zachary Manchester⁵

Abstract—We present Dojo, a differentiable physics engine for robotics that prioritizes stable simulation, accurate contact physics, and differentiability with respect to states, actions, and system parameters. Dojo achieves stable simulation at low sample rates and conserves energy and momentum by employing a variational integrator. A nonlinear complementarity problem with second-order cones for friction models hard contact, and is reliably solved using a custom primal-dual interior-point method. Special properties of the interior-point method are exploited using implicit differentiation to efficiently compute smooth gradients that provide useful information through contact events. We demonstrate Dojo with a number of examples including: planning, policy optimization, and system identification, that demonstrate the engine’s unique ability to simulate hard contact while providing smooth, analytic gradients.

Index Terms—Contact Dynamics, Differentiable Optimization, Simulation, Robotics

I. INTRODUCTION

The last decade has seen immense advances in learning-based methods for policy optimization and trajectory optimization in robotics, e.g., for dexterous manipulation [2, 1], quadrupedal locomotion [22, 20], and pixels-to-torques control [23]. These advances have largely hinged on innovations in learning architectures, large scale optimization algorithms, and large datasets. In contrast, there has been comparatively little work on the lowest level of the robotics reinforcement learning stack: the *physics engine*. We argue that deficiencies in current widely used physics engines form a key bottleneck that must be overcome to enable future advancements in robotics.

Physics engines that simulate rigid-body dynamics with contact are utilized for trajectory optimization, reinforcement learning, system identification, and dataset generation for domains ranging from locomotion to manipulation. To overcome the sim-to-real gap [46] and to be of practical value in real-world applications, an engine should provide stable simulation, accurately reproduce a robot’s dynamics, and ideally, be differentiable to enable the use of efficient gradient-based optimization methods.

¹ Taylor A. Howell and Simon Le Cleac’h are with the Department of Mechanical Engineering, Stanford University, Stanford, CA 94305, USA. {thowell, simonlc}@stanford.edu

² Jan Brüdigam is with the School of Computation, Information and Technology, Technical University of Munich, Munich, 80333, Germany. jan.brueedigam@tum.de

³ J. Zico Kolter is with the Department of Computer Science, Carnegie Mellon University, Pittsburgh, PA 15213, USA. zkolter@cs.cmu.edu

⁴ Mac Schwager is with the Department of Aeronautics and Astronautics, Stanford University, Stanford, CA 94305, USA. schwager@stanford.edu

⁵ Zachary Manchester is with The Robotics Institute, Carnegie Mellon University, Pittsburgh, PA 15213, USA. zacm@cmu.edu

(Corresponding authors: T. Howell, S. Le Cleac’h)

* These authors contributed equally to this work.

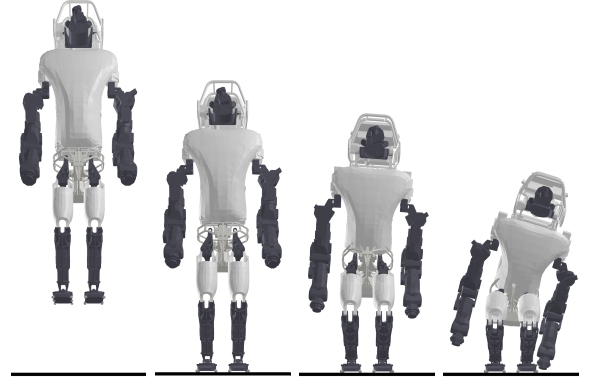


Fig. 1: Atlas drop simulation. Dojo simulates this system with 403 maximal-coordinates states, 30 joint constraints, 36 inputs, and 8 contact points in real-time at 65 Hz. Dojo respects floor-feet penetration constraints to machine precision, while MuJoCo suffers from centimeters of interpenetration and is unstable at such low simulation rates.

In recent years, a number of physics engines [41, 13, 45, 14, 17, 15] have been developed and utilized for robotics. In this work, we address key deficiencies of these tools including: (i) high sample rates required for stable simulation that exacerbate the vanishing/exploding gradient problem and substantially increase sample complexities for rollout-based optimization methods, (ii) artifacts like interpenetration of rigid bodies (e.g., a robot foot sinking through the floor) and creep (e.g., objects that should be at rest incorrectly sliding), and (iii) lack of informative gradients through contact events (e.g., subgradients resulting from naïve differentiation of non-smooth dynamics) or expensive gradients that require a large number of calls to the engine (e.g. finite-difference or stochastic-sampling schemes).

The Dojo physics engine is designed from the ground up to address these three key deficiencies, enabling better and easier optimization for motion planning, control, reinforcement learning, system identification, and high-quality dataset generation. By taking a physics- and optimization-first approach to physics-engine design, we advance the state of the art in *stable simulation*, *accurate contact physics*, and *differentiability* for robot simulation. Key attributes of Dojo include:

- Variational integration for stable simulation that is not sensitive to timestep size
- A nonlinear complementarity problem (NCP) model for accurate contact dynamics
- A custom primal-dual interior-point method for reliably solving the NCP

TABLE I: Comparison of physics engines used for robotics.

Engine	Application	Integrator	State	Contact Type	Contact Solver	Gradients
MuJoCo	robotics	RK4	minimal	soft	Newton	finite difference
Drake	robotics	implicit Euler	minimal	soft/hard	LCP	randomized smoothing
Bullet	graphics	implicit Euler	minimal	soft/hard	LCP	subgradient
DART	robotics	implicit Euler	minimal	hard	LCP	subgradient
PhysX	graphics	explicit	minimal	soft	iterative	finite difference
Brax	graphics	explicit	maximal	soft	iterative	subgradient
Dojo	robotics	variational	maximal	hard	NCP	implicit gradient

- Smooth, analytic gradients through contact efficiently computed via implicit differentiation of the interior-point solver

In the remainder of this paper, we first provide an overview of related state-of-the-art physics engines in Section II. We then summarize important technical background in Section III. Next, we present Dojo, and its key features in Section IV. Simulation, planning, policy optimization, and system identification examples are presented in Section V. Finally, we conclude with a discussion of limitations and future work in Section VI.

II. RELATED WORK

This section provides an overview of physics engines that are commonly used in robotics. Table I summarizes the features of these tools and compares them to Dojo.

Many physics engines being developed and used in practice today were not designed for real-world robotics applications, and it is common for these tools to prioritize the *appearance* of realism over actual physical accuracy. Additionally, many of these physics engines were designed primarily for graphics and animation applications where fast simulation rates are prioritized and general-purpose numerical-optimization routines that do not natively support key elements from robotics domains, like cone constraints or quaternions, are commonplace. In this section, we provide background on a collection of popular existing state-of-the-art physics engines, including: discussion of physical fidelity, underlying optimization routines, and ability to return gradients.

In the learning community, *MuJoCo* [43] has become a standard for benchmarking reinforcement learning algorithms using the OpenAI Gym environments [4]. *MuJoCo* utilizes minimal-coordinates representations, and employs both semi-implicit Euler and explicit fourth-order Runge-Kutta integrators to simulate multi-body systems. These integrators often require small time steps, particularly for systems experiencing contact, and typically sample rates of hundreds to thousands of Hertz are required for stable simulation, which a mature and efficient implementation is able to achieve at much faster than real-time rates. However, these high rates can prove a challenge for control tasks, such as reinforcement learning settings where vanishing or exploding gradients are exacerbated over long horizons with many time steps.

Impact and friction are modeled using a smooth, convex contact model [42]. While this approach reliably computes contact forces, it introduces unphysical artifacts, allowing the system to experience interpenetration and contact forces

at a distance (i.e., while not in contact), and the default friction model introduces creep and velocity drift during sliding. Additionally, achieving good simulation behavior often requires system-specific tuning of multiple solver parameters. Further, the “soft” contact model is computed using a *primal* optimization method, meaning that as parameters are set to produce “hard,” or more realistic contact, the underlying optimization problem becomes increasingly ill-conditioned and difficult to solve. As a result, it is often not possible to eliminate unphysical artifacts from the simulation to produce realistic results. The lack of smooth gradients is also a major challenge in deep learning [34], where contact dynamics must be smoothed unrealistically much to make learning progress.

Analytical gradients are not provided by the engine, and instead require finite-difference schemes [40] that are computationally expensive. This approach requires multiple calls to the engine, which can be expensive if not performed in parallel.

Drake [41] was designed for robotics applications and follows a principled approach prioritizing physical accuracy. Its contact dynamics primarily rely on a classic time-stepping contact model that solves a linear complementarity problem (LCP) at each time step [38]. To satisfy the LCP problem formulation, a number of approximations are made to the dynamics and contact model, including the use of an approximate friction cone. To ensure stability of the simulation, small time steps are used where linearizations of the dynamics are valid, but importantly, the engine can achieve accurate hard contact. General-purpose LCP solvers that are typically used rely on a pivoting method like Lemke’s algorithm [7]. Randomized smoothing has been proposed as a method for returning gradients through contact [39] with this model. The engine also includes an alternative soft-contact model for patch contacts [11], but it is more computationally expensive, requiring sophisticated higher-order implicit integrators, and does not natively provide gradients.

The popular robotics simulator *Gazebo* [19] can utilize several different physics engines to simulate multi-body contact dynamics, *Bullet* [8] and *DART* [21] are common choices. Similar to *Drake*, these engines model hard contact dynamics with an LCP formulation. Automatic differentiation tools have been utilized to compute gradients [15]. However, because of the discontinuous nature of contact dynamics, this approach will return subgradients, which do not provide useful information through contact events. Heuristics have been proposed to enumerate contact modes in order to select informative subgradients [45]. However, this approach scales poorly with the number of contact mode switches.

Engines designed for hardware accelerators (e.g., GPUs), including *Brax* [13] and *PhysX* [33], typically utilize simplified contact dynamics. Additionally, these engines usually require system-specific tuning and their simulation results are typically lower fidelity.

The properties and characteristics of these existing engines are summarized in Table I. We find that none of the existing engines prioritize two of the most important attributes for robotics: physical accuracy and useful differentiability. This motivates our development of a new physics engine for robotics applications.

Building on prior work [6], Dojo utilizes the open-source maximal-coordinates dynamics library `ConstrainedDynamics.jl` and efficient graph-based linear-system solver `GraphBasedSystems.jl`. However, unlike this previous work, Dojo has an improved contact model, specifically with regard to friction; and utilizes a more efficient, reliable, and versatile interior-point solver for the NCP.

III. BACKGROUND

This section provides important background information on complementarity-based contact models and implicit differentiation.

A. Complementarity-Based Contact Models

Impacts and friction can be modeled through constraints on the system's configuration and the applied contact impulses.

Impact: For a system with P contact points, we define a signed-distance function, $\phi : \mathbf{Z} \rightarrow \mathbf{R}^P$, subject to the following element-wise constraint:

$$\phi(z) \geq 0. \quad (1)$$

Impact forces with magnitude $\gamma \in \mathbf{R}^P$ are applied to the bodies' contact points in the direction of their surface normals in order to enforce (1) and prevent interpenetration. A non-negative constraint:

$$\gamma \geq 0, \quad (2)$$

enforces physical behavior that impulses are repulsive (e.g., the floor does not attract bodies), and the complementarity condition:

$$\gamma \circ \phi(z) = 0, \quad (3)$$

where \circ is an element-wise product operator, enforces zero force if the body is not in contact and allows non-zero force during contact.

Friction: Coulomb friction instantaneously maximizes the dissipation of kinetic energy between two objects in contact. For a single contact point, this physical phenomenon can be modeled by the following optimization problem:

$$\begin{aligned} & \underset{b}{\text{minimize}} && v^T b \\ & \text{subject to} && \|b\|_2 \leq c_f \gamma, \end{aligned} \quad (4)$$

where $v \in \mathbf{R}^2$ is the tangential velocity at the contact point, $b \in \mathbf{R}^2$ is the friction force, and $c_f \in \mathbf{R}_+$ is the coefficient of friction between the two objects [31].



Fig. 2: Friction-cone comparison. Linearized double-parameterized (left) and nonlinear second-order (right) cones.

This problem is naturally a convex second-order cone program, and can be efficiently and reliably solved [25]. Classically, other works solve an approximate version of (4):

$$\begin{aligned} & \underset{\beta}{\text{minimize}} && [v^T \quad -v^T] \beta \\ & \text{subject to} && \beta^T \mathbf{1} \leq c_f \gamma, \\ & && \beta \geq 0, \end{aligned} \quad (5)$$

which satisfies the LCP formulation, is instead solved. Here, the friction cone is linearized (Fig. 2) and the friction vector, $\beta \in \mathbf{R}^4$, is correspondingly overparameterized and subject to additional positivity constraints [38].

The optimality conditions of (5) and constraints used in the LCP are:

$$[v^T \quad -v^T]^T + \psi \mathbf{1} - \eta = 0, \quad (6)$$

$$c_f \gamma - \beta^T \mathbf{1} \geq 0, \quad (7)$$

$$\psi \cdot (c_f \gamma - \beta^T \mathbf{1}) = 0, \quad (8)$$

$$\beta \circ \eta = 0, \quad (9)$$

$$\beta, \psi, \eta \geq 0, \quad (10)$$

where $\psi \in \mathbf{R}$ and $\eta \in \mathbf{R}^4$ are the dual variables associated with the friction cone and positivity constraints, respectively, and $\mathbf{1}$ is a vector of ones.

The primary drawback of this formulation is that the optimized friction force will naturally align with the vertices of the cone approximation, which may not align with the velocity vector of the contact point. Thus, the friction force does not perfectly oppose the movement of the system at the contact point. Unless the pyramidal approximation is improved with a finer discretization, incurring increased computational cost, unphysical velocity drift will occur. Additionally, the LCP contact model requires a linearized form of the dynamics (12) and a linear approximation of the signed-distance functions (1-3), both of which negatively impact physical accuracy.

B. Implicit Differentiation

An implicit function, $r : \mathbf{R}^{n_w} \times \mathbf{R}^{n_\theta} \rightarrow \mathbf{R}^{n_w}$, is defined as $r(w^*; \theta) = 0$ for solution $w^* \in \mathbf{R}^{n_w}$ and problem data $\theta \in \mathbf{R}^{n_\theta}$. At a solution point, the sensitivities of the solution with respect to the problem data, i.e., $\partial w^* / \partial \theta$, can be computed using the implicit function theorem [9]:

$$\frac{\partial w^*}{\partial \theta} = - \left(\frac{\partial r}{\partial w} \right)^{-1} \frac{\partial r}{\partial \theta}. \quad (11)$$

Newton's method is typically employed to find solutions w^* . When the method succeeds, the sensitivity (11) can be computed and the factorization of $\partial r / \partial w$ used to find the solution is reused to efficiently compute sensitivities at

very low computational cost, using only back-substitution. Additionally, each element of the sensitivity can be computed in parallel.

IV. DOJO

We now introduce Dojo's contact dynamics model and custom interior-point solver. This section presents the key algorithms and subroutines, including: maximal-coordinates representation, variational integrators, contact model, primal-dual interior-point solver, and smooth gradients. An open-source implementation of the engine is provided.

A. Maximal-Coordinates State Representation

Most multi-body physics engines utilize minimal- or joint-coordinate representations for dynamics because of the small number of states and convenience of implementation. This results in small, but dense, systems of equations. In contrast, maximal-coordinates explicitly represent the position, orientation, and velocities of each body in a multi-body system. This produces large, sparse systems of equations that can be efficiently solved, including in the contact setting. We provide an overview, largely based on prior work [5], of this representation.

A single rigid body is defined by its mass and inertia, and has a configuration, $x = (p, q) \in \mathbf{X} = \mathbf{R}^3 \times \mathbf{H}$, comprising a position p and unit quaternion q , where \mathbf{H} is the space of four-dimensional unit quaternions. We define the implicit discrete-time dynamics $F : \mathbf{X} \times \mathbf{X} \times \mathbf{X} \rightarrow \mathbf{R}^6$ as:

$$F(x_-, x, x_+) = 0, \quad (12)$$

where we indicate the previous and next time steps with minus (−) and plus (+) subscripts, respectively, and the current time step without decoration. We employ a variational integrator that has desirable energy and momentum conservation properties [29]. Linear and angular velocities are handled implicitly via finite-difference approximations.

For a two-body system with bodies a and b connected via a joint—common types include revolute, prismatic, and spherical—we introduce a constraint, $k : \mathbf{X} \times \mathbf{X} \rightarrow \mathbf{R}^l$, that couples the two bodies:

$$k^{ab}(x_+^a, x_+^b) = 0. \quad (13)$$

An impulse, $j \in \mathbf{R}^l$, where l is equal to the six degrees-of-freedom of an unconstrained body minus the joint's number of degrees-of-freedom, acts on both bodies to satisfy the constraint. The implicit integrator for the two-body system has the form:

$$\begin{bmatrix} F^a(x_-^a, x^a, x_+^a) + K^a(x^a, x^b)^T j^{ab} \\ F^b(x_-^b, x^b, x_+^b) + K^b(x^a, x^b)^T j^{ab} \\ k^{ab}(x_+^a, x_+^b) \end{bmatrix} = 0, \quad (14)$$

where $K : \mathbf{X} \times \mathbf{X} \rightarrow \mathbf{R}^{l \times 6}$ is a mapping from the joint to the maximal-coordinates space and is related to the Jacobian of the joint constraint.

We can generalize (14) to include additional bodies and joints. For a multi-body system with N bodies and M joints we define a maximal-coordinates configuration $z =$

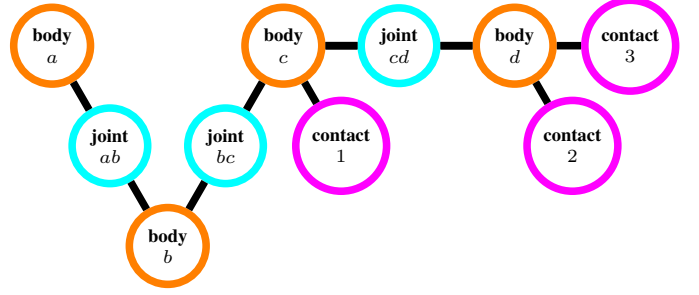


Fig. 3: Graph structure for maximal-coordinates system with 4 bodies, 3 joints, and 3 points of contact.

$(x^{(1)}, \dots, x^{(N)}) \in \mathbf{Z}$ and joint impulse $j = (j^{(1)}, \dots, j^{(M)}) \in \mathbf{J}$. We define the implicit discrete-time dynamics of the maximal-coordinates system as:

$$F(z_-, z, z_+, j) = 0, \quad (15)$$

where $F : \mathbf{Z} \times \mathbf{Z} \times \mathbf{Z} \times \mathbf{J} \rightarrow \mathbf{R}^{6N}$. In order to simulate the system we find z_+ and j that satisfy (15) for a provided z_- and z using Newton's method.

By exploiting the mechanism's structure, we can efficiently perform root finding on (15) (see [5] for additional details). This structure is manifested as a graph of the mechanism, where each body and joint is considered a node, and joints have edges connecting bodies (Fig. 3). Because the mechanism structure is known *a priori*, a permutation matrix can be precomputed and used to perform efficient sparse linear algebra during simulation. For instance, in the case where the joint constraints form a system without loops, the resulting sparse system can be solved in linear time with respect to the number of links.

B. Variational Integrator

We use a specialized implicit integrator that preserves energy and momentum, natively handles quaternions, and alleviates spurious artifacts that commonly arise from contact interactions. Dojo utilizes a maximal-coordinates state representation [5]. The dynamics are derived by approximating Hamilton's Principle of Least-Action using a simple midpoint scheme [29, 26]. This approach produces *variational* integrators that automatically conserve momentum and energy [29].

Each body has linear:

$$m \frac{p_+ - 2p + p_-}{h} - hmg - A(p)^T j - hf = 0, \quad (16)$$

and rotational:

$$\begin{aligned} & \sqrt{1 - \psi_+^T \psi_+} J \psi_+ + \psi_+ \times J \psi_+ \\ & - \sqrt{1 - \psi^T \psi} J \psi + \psi \times J \psi - B(q)^T j - h^2 \frac{T}{2} = 0, \end{aligned} \quad (17)$$

dynamics specified by mass $m \in \mathbf{R}_{++}$, inertia $J \in \mathbf{S}_{++}^3$, gravity $g \in \mathbf{R}^3$, and time step $h \in \mathbf{R}_{++}$. Equations (16, 17) are essentially second-order centered-finite-difference approximations of Newton's second law and Euler's equation for the rotational dynamics, respectively, where:

$$q_+ = q \cdot \begin{bmatrix} \sqrt{1 - \psi_+^T \psi_+} \\ \psi_+ \end{bmatrix} \quad (18)$$

Algorithm 1 Analytical Line Search For Cones

```

1: procedure SEARCH( $w, \Delta, \tau^{\text{ort}}, \tau^{\text{soc}}$ )
2:    $\alpha_y^{\text{ort}} \leftarrow \alpha(y^{(1)}, \tau^{\text{ort}} \Delta y^{(1)})$  ▷ 41
3:    $\alpha_z^{\text{ort}} \leftarrow \alpha(z^{(1)}, \tau^{\text{ort}} \Delta z^{(1)})$  ▷ 41
4:    $\alpha_y^{\text{soc}} \leftarrow \min_{i \in \{2, \dots, n\}} \alpha(y^{(i)}, \tau^{\text{soc}} \Delta y^{(i)})$  ▷ 46
5:    $\alpha_z^{\text{soc}} \leftarrow \min_{i \in \{2, \dots, n\}} \alpha(z^{(i)}, \tau^{\text{soc}} \Delta z^{(i)})$  ▷ 46
6:   Return  $\min(\alpha_y^{\text{ort}}, \alpha_z^{\text{ort}}, \alpha_y^{\text{soc}}, \alpha_z^{\text{soc}})$ 

```

is recovered from a three-parameter representation $\psi \in \mathbf{R}^3$ [27]. We refer to Appendix A for quaternion conventions and algebra. Joint impulses $j \in \mathbf{J}$ have linear $A : \mathbf{R}^3 \rightarrow \mathbf{R}^{\dim(\mathbf{J}) \times 3}$ and rotational $B : \mathbf{H} \rightarrow \mathbf{R}^{\dim(\mathbf{J}) \times 3}$ mappings into the dynamics. The configuration of a body $x^{(i)} = (p^{(i)}, q^{(i)}) \in \mathbf{R}^3 \times \mathbf{H}$ comprises a position and orientation represented as a quaternion. Forces and torques $f, \tau \in \mathbf{R}^3$ can be applied to the bodies.

C. Contact Dynamics Model

Impact and friction behaviors are modeled, along with the system's dynamics, as an NCP. This model simulates hard contact without requiring system-specific solver tuning. Additionally, contacts between a system and the environment are treated as a single graph node connected to a rigid body (Fig 3). As a result, the engine retains efficient linear-time complexity for open-chain mechanical systems.

Dojo uses the rigid impact model (1-3) and in the following section we present its Coulomb friction model that utilizes an exact nonlinear friction cone.

Nonlinear friction cone: In contrast to the LCP approach, we utilize the optimality conditions of (4) in a form amenable to a primal-dual interior-point solver. The associated cone program is:

$$\begin{aligned}
& \underset{\beta}{\text{minimize}} && v^T \beta_{(2:3)} \\
& \text{subject to} && \beta_{(1)} = c_f \gamma, \\
& && \|\beta_{(2:3)}\|_2 \leq \beta_{(1)},
\end{aligned} \tag{19}$$

where subscripts indicate vector indices. The relaxed optimality conditions for (19) in interior-point form are:

$$v - \eta_{(2:3)} = 0, \tag{20}$$

$$\beta_{(1)} - c_f \gamma = 0, \tag{21}$$

$$\beta \circ \eta = \kappa \mathbf{e}, \tag{22}$$

$$\|\beta_{(2:3)}\|_2 \leq \beta_{(1)}, \|\eta_{(2:3)}\|_2 \leq \eta_{(1)}, \tag{23}$$

with dual variable $\eta \in \mathbf{R}^3$ associated with the second-order-cone constraints, and central-path parameter, $\kappa \in \mathbf{R}_+$. The second-order-cone product is:

$$\beta \circ \eta = (\beta^T \eta, \beta_{(1)} \eta_{(2:n)} + \eta_{(1)} \beta_{(2:n)}), \tag{24}$$

and:

$$\mathbf{e} = (1, 0, \dots, 0), \tag{25}$$

is its corresponding identity element [44]. Friction is recovered from the solution: $b = \beta_{(2:3)}^*$. The benefits of this model are

Algorithm 2 Primal-Dual Interior-Point Solver

```

1: procedure OPTIMIZE( $a_0, b_0, c_0, \theta, \mathcal{K}$ )
2:   Parameters:  $\tau_{\text{max}}^{\text{soc}} = 0.99, \tau_{\text{min}} = 0.95$ 
3:    $r_{\text{tol}} = 10^{-5}, \kappa_{\text{tol}} = 10^{-5}, \beta = 0.5$ 
4:   Initialize:  $a = a_0, b = b_0 \in \mathcal{K}, c = c_0 \in \mathcal{K}$ 
5:    $r_{\text{vio}}, \kappa_{\text{vio}} \leftarrow \text{VIOLATION}(w)$  ▷ (49, 50)
6:   Until  $r_{\text{vio}} < r_{\text{tol}}$  and  $\kappa_{\text{vio}} < \kappa_{\text{tol}}$  do
7:      $\Delta^{\text{aff}} \leftarrow -\bar{R}^{-1}(w; \theta) r(w; \theta, 0)$ 
8:      $\alpha^{\text{aff}} \leftarrow \text{CONESearch}(w, \Delta^{\text{aff}}, 1, 1)$ 
9:      $\mu, \sigma \leftarrow \text{CENTER}(b, c, \alpha^{\text{aff}}, \Delta^{\text{aff}})$  ▷ (51-54)
10:     $\kappa \leftarrow \max(\sigma \mu, \kappa_{\text{tol}}/5)$ 
11:     $\Delta \leftarrow -\bar{R}^{-1}(w; \theta) r(w; \theta, \kappa)$ 
12:     $\tau^{\text{ort}} \leftarrow \max(\tau_{\text{min}}, 1 - \max(r_{\text{vio}}, \kappa_{\text{vio}})^2)$ 
13:     $\tau^{\text{soc}} \leftarrow \min(\tau_{\text{max}}^{\text{soc}}, \tau^{\text{ort}})$ 
14:     $\alpha \leftarrow \text{CONESearch}(w, \Delta, \tau^{\text{ort}}, \tau^{\text{soc}})$ 
15:     $c_{\text{vio}}^*, \kappa_{\text{vio}}^* \leftarrow r_{\text{vio}}, \kappa_{\text{vio}}$ 
16:     $\hat{w} \leftarrow \text{UPDATE}(w, \Delta, \alpha)$  ▷ (47, 48)
17:     $r_{\text{vio}}, \kappa_{\text{vio}} \leftarrow \text{VIOLATION}(\hat{w})$  ▷ (49, 50)
18:    Until  $r_{\text{vio}} \leq c_{\text{vio}}^*$  or  $\kappa_{\text{vio}} \leq \kappa_{\text{vio}}^*$  do
19:       $\alpha \leftarrow \beta \alpha$ 
20:       $\hat{w} \leftarrow \text{UPDATE}(w, \Delta, \alpha)$  ▷ (47, 48)
21:       $r_{\text{vio}}, \kappa_{\text{vio}} \leftarrow \text{VIOLATION}(\hat{w})$  ▷ (49, 50)
22:    end
23:     $w \leftarrow \hat{w}$ 
24:  end
25:   $\partial w^* / \partial \theta \leftarrow -\bar{R}^{-1}(w^*; \theta) \bar{D}(w^*; \theta)$  ▷ (11)
26:  Return  $w, \partial w^* / \partial \theta$ 

```

increased physical fidelity and fewer optimization variables, without substantial increase in computational cost.

Nonlinear complementarity problem: Systems comprising N bodies and a single contact point are simulated using a time-stepping scheme that solves the feasibility problem:

$$\begin{aligned}
& \text{find} && z_+, j, \gamma, \beta, \eta \\
& \text{subject to} && F(z_-, z, z_+, j, \gamma, \beta, u) = 0, \\
& && \gamma \circ \phi(z_+) = \kappa \mathbf{1}, \\
& && \beta \circ \eta = \kappa \mathbf{e}, \\
& && v(z, z_+) - \eta_{(2:3)} = 0, \\
& && \beta_{(1)} - c_f \gamma = 0, \\
& && \gamma, \phi(z_+) \geq 0, \\
& && \|\beta_{(2:3)}\|_2 \leq \beta_{(1)}, \|\eta_{(2:3)}\|_2 \leq \eta_{(1)}.
\end{aligned} \tag{26}$$

The system's smooth dynamics $F : \mathbf{Z} \times \mathbf{Z} \times \mathbf{Z} \times \mathbf{J} \times \mathbf{R}_+ \times \mathbf{R}^2 \times \mathbf{U} \rightarrow \mathbf{R}^{6N}$ comprise linear and rotational dynamics (16-17) for each body which are subject to inputs $u = (f^{(1)}, \tau^{(1)}, \dots, f^{(N)}, \tau^{(N)}) \in \mathbf{U}$. The contact-point tangential velocity $v : \mathbf{Z} \times \mathbf{Z} \rightarrow \mathbf{R}^2$ is a function of the current and next configurations (i.e., a finite-difference velocity). The central-path parameter $\kappa \in \mathbf{R}_+$ and target \mathbf{e} [44] are utilized by the interior-point solver in the following section. This formulation extends to multiple contacts.

Solving the NCP finds a maximal-coordinates state representation. In many applications it is desirable to utilize a minimal-coordinates representation (e.g., direct trajectory

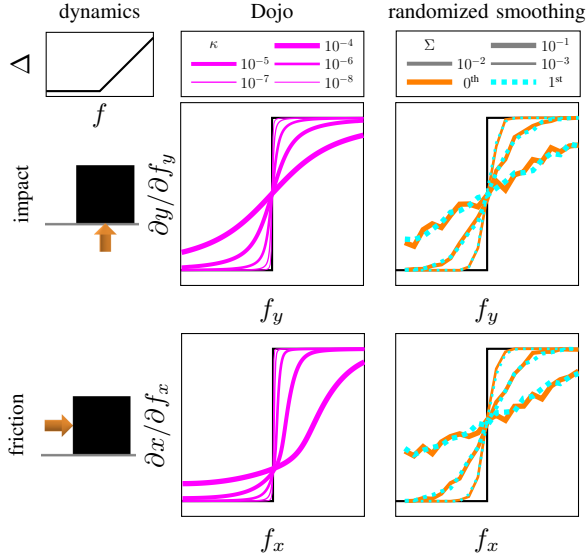


Fig. 4: Gradient comparison between subgradients (black), randomized-smoothing gradients [39] (orange, blue) and Dojo’s analytic gradients (magenta). The dynamics for a box in the XY plane that is resting on a flat surface and displaced an amount Δ by a force f (top left). Randomized smoothing gradients (right column) are computed using 500 samples with varying covariances Σ . Dojo’s gradients (middle column) are computed for different values of central-path parameter κ . Compared to Dojo, the randomized smoothing method produces noisy derivatives that are many times more expensive to compute.

optimization where algorithm complexity scales with the state dimension). Dojo includes functionality to analytically convert between representations, as well as formulate and apply the appropriate chain rule in order to differentiate through a representation transformation.

To simulate a system forward in time one step, given a control input and state comprising the previous and current configurations, solutions to a sequence of barrier problems (26) are found with $\kappa \rightarrow 0$. The central-path parameter has a physical interpretation as being the softness of the contact model. A value $\kappa = 0$ corresponds to exact “hard” or inelastic contact, whereas a relaxed value produces soft contact where contact forces can occur at a distance. The primal-dual interior-point solver described in the next section adaptively decreases this parameter in order to efficiently and reliably converge to hard contact solutions. In practice, the engine is set to converge to small values for simulation in order to simulate accurate physics. Intermediate solutions (i.e., $\kappa \neq 0$) are cached and later utilized to compute smooth gradients in order to provide useful information through contact events.

D. Primal-Dual Interior-Point Solver

To efficiently and reliably satisfy (26), we developed a custom primal-dual interior-point solver for NCPs with support for cone constraints and quaternions. The algorithm is largely based upon Mehrotra’s predictor-corrector algorithm [30, 32], while implementing non-Euclidean optimization techniques to handle quaternions [18] and borrowing features from CVX-OPT [44] to handle cones.

TABLE II: Contact violation for Atlas drop. Comparison between Dojo and MuJoCo for foot contact penetration (millimeters) with the floor for different time steps (seconds). Dojo strictly enforces no penetration. When Atlas lands, its feet remains above the ground by an infinitesimal amount. In contrast, MuJoCo exhibits significant penetration through the floor (i.e., negative values).

Time Step	0.1	0.01	0.001
MuJoCo	failure	-28	-46
Dojo	+1e-12	+1e-7	+8e-6

The primary advantages of this algorithm are the correction to the classic Newton step, which can greatly reduce the iterations required by the solver (often halving the total number of iterations), and feedback on the problem’s central-path parameter that helps avoid premature ill-conditioning and adaptively drives the complementarity violation to zero in order to reliably simulate hard contact.

Problem formulation: The solver aims to satisfy instantiations of the following problem:

$$\begin{aligned} &\text{find} && a, b, c \\ &\text{subject to} && E(a, b, c; \theta) = 0, \\ & && b \circ c = \kappa \mathbf{e}, \\ & && b, c \in \mathcal{K}, \end{aligned} \quad (27)$$

with decision variables $a \in \mathbf{R}^{n_a}$ and $b, c \in \mathbf{R}^{n_\kappa}$, equality-constraint set $E : \mathbf{R}^{n_a} \times \mathbf{R}^{n_\kappa} \times \mathbf{R}^{n_\kappa} \times \mathbf{R}^{n_\theta} \rightarrow \mathbf{R}^{n_a+n_\kappa}$, problem data $\theta \in \mathbf{R}^{n_\theta}$; and where \mathcal{K} is the Cartesian product of positive-orthant and second-order cones [3].

Interior-point methods aim to satisfy a sequence of relaxed problems with $\kappa > 0$ and $\kappa \rightarrow 0$ in order to reliably converge to a solution of the original problem (i.e., $\kappa = 0$). This continuation approach helps avoid premature ill-conditioning and is the basis for numerous convex and non-convex interior-point solvers [32].

The LCP formulation is a special-case instantiation of (27) where the constraint set is affine in the decision variables and the cone is the positive orthant. Most general-purpose solvers for LCP problems rely on active-set methods that strictly enforce $\kappa = 0$ at each iteration. Consequently, these solvers generate non informative gradient information (see Section IV-E).

Residual and Jacobians: The interior-point solver aims to find a fixed point for the residual:

$$r(w; \theta, \kappa) = \begin{bmatrix} E(w; \theta) \\ b^{(1)} \circ c^{(1)} - \kappa \mathbf{1} \\ \vdots \\ b^{(n_\kappa)} \circ c^{(n_\kappa)} - \kappa \mathbf{e} \end{bmatrix}, \quad (28)$$

while respecting the cone constraints. The Jacobian of this residual with respect to the decision variables:

$$R(w; \theta) = \frac{\partial r(w; \theta, \cdot)}{\partial w}, \quad (29)$$

is used to compute a search direction. For convenience, we denote $w = (a, b, c)$. After a solution $w^*(\theta, \kappa)$ is found, the Jacobian of the residual with respect to the problem data:

$$D(w; \theta) = \frac{\partial r(w; \theta, \cdot)}{\partial \theta}, \quad (30)$$

TABLE III: Compute-time ratio between Dojo’s maximal-coordinates gradient and simulation-step evaluations for a variety of robots. We compute the engine’s implicit gradient with respect to the initial configuration, velocity and control input. For a large system like Atlas, using a finite-difference (FD) scheme to evaluate the dynamics Jacobian in maximal coordinates would require at least 400 simulation-step evaluations. Alternatively, Dojo computes this Jacobian at the cost of approximately 4 simulation-step evaluations: a potential 100 times speedup on a single thread.

	Atlas	Humanoid	Quadruped	Ant	Half-Cheetah
Dojo	3.7	4.9	2.5	2.3	1.2
FD	472.6	194.7	170.3	197.0	94.8

is used to compute the sensitivity of the solution. These Jacobians are not explicitly dependent on the central-path parameter.

The non-Euclidean properties of quaternion variables are handled with modifications to these Jacobians (29) and (30) by right multiplying each with a matrix H containing attitude Jacobians [18] corresponding to the quaternions in x and θ , respectively:

$$\bar{R}(w; \theta) = R(w; \theta)H_R(w), \quad (31)$$

$$\bar{D}(w; \theta) = D(w; \theta)H_D(\theta). \quad (32)$$

Euclidean variables have corresponding identity blocks. This modification accounts for the implicit unit-norm constraint on each quaternion variable and improves the convergence behaviour of the solver.

Cones: The generalized inequality, cone-product operator, and target for the n -dimensional positive orthant are:

$$\mathbf{R}_{++}^n = \{a \in \mathbf{R}^n \mid a_{(i)} > 0, i = 1, \dots, n\}, \quad (33)$$

$$a \circ b = (a_{(1)}b_{(1)}, \dots, a_{(n)}b_{(n)}), \quad (34)$$

$$\mathbf{e} = \mathbf{1}. \quad (35)$$

For the second-order cone they are:

$$\mathcal{Q}^n = \{(a_{(1)}, a_{(2:n)}) \in \mathbf{R} \times \mathbf{R}^{n-1} \mid \|a_{(2:n)}\|_2 \leq a_{(1)}\}, \quad (36)$$

$$a \circ b = (a^T b, a_{(1)}b_{(2:n)} + a_{(1)}b_{(2:n)}), \quad (37)$$

$$\mathbf{e} = (1, 0, \dots, 0). \quad (38)$$

The solver utilizes the Cartesian product:

$$\mathcal{K} = \mathbf{R}_{++}^n \times \mathcal{Q}_1^{l_1} \times \dots \times \mathcal{Q}_j^{l_j}, \quad (39)$$

of the n -dimensional positive orthant and j second-order cones, each of dimension l_i .

Analytical line search for cones: To ensure the cone variables strictly satisfy their constraints, a cone line search is performed for a candidate search direction. For the update:

$$y \leftarrow y + \alpha \Delta, \quad (40)$$

with step size α and search direction Δ , the solver finds the largest $\alpha \in [0, 1]$ such that $y + \alpha \Delta \in \mathcal{K}$. The step-size is computed analytically for the positive orthant:

$$\alpha = \min \left(1, \max_{k \mid \Delta_{(k)} < 0} \left\{ -\frac{y_{(k)}}{\Delta_{(k)}} \right\} \right), \quad (41)$$

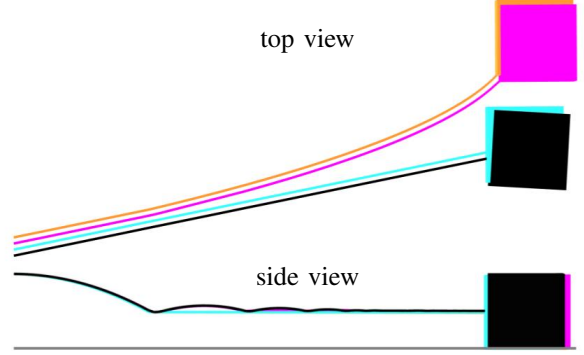


Fig. 5: Velocity drift resulting from friction-cone approximation. Comparison between a box sliding with approximate cones having four vertices implemented in MuJoCo (magenta) and Dojo (orange) versus MuJoCo’s (black) and Dojo’s (blue) nonlinear friction cones. Dojo’s nonlinear friction cone gives the physically correct straight line motion, while linear friction-cone approximations lead to lateral drift. MuJoCo’s nonlinear friction cone exhibits a minor rotational drift.

and second-order cone:

$$\nu = y_{(1)}^2 - y_{(2:k)}^T y_{(2:k)}, \quad (42)$$

$$\zeta = y_{(1)} \Delta_{(1)} - y_{(2:k)}^T \Delta_{(2:k)}, \quad (43)$$

$$\rho_{(1)} = \frac{\zeta}{\nu}, \quad (44)$$

$$\rho_{(2:k)} = \frac{\Delta_{(2:k)}}{\sqrt{\nu}} - \frac{\frac{\zeta}{\sqrt{\nu}} + \Delta_{(1)}}{y_{(1)}\sqrt{\nu} + \nu} y_{(2:k)}, \quad (45)$$

$$\alpha = \begin{cases} \min \left(1, \frac{1}{\|\rho_{(2:k)}\|_2 - \rho_{(1)}} \right), & \|\rho_{(2:k)}\|_2 > \rho_{(1)}, \\ 1, & \text{otherwise.} \end{cases} \quad (46)$$

The line search over all individual cones is summarized in Algorithm 1.

Candidate update: The variables are partitioned: $a = (a^{(1)}, \dots, a^{(p)})$, where $i = 1$ are Euclidean variables and $i = 2, \dots, p$ are each quaternion variables; and $b = (b^{(1)}, \dots, b^{(n)})$, $c = (c^{(1)}, \dots, c^{(n)})$, where $j = 1$ is the positive-orthant and the remaining $j = 2, \dots, n$ are second-order cones. For a given search direction, updates for Euclidean and quaternion variables are performed. The Euclidean variables in a use a standard update:

$$a^{(1)} \leftarrow a^{(1)} + \alpha \Delta^{(1)}, \quad (47)$$

For each quaternion variable, the search direction exists in the space tangent to the unit-quaternion hypersphere and is 3-dimensional. The corresponding update for $i = 2, \dots, p$ is:

$$a^{(i)} \leftarrow L(a^{(i)})\varphi(\alpha \Delta^{(i)}), \quad (48)$$

where $L : \mathbf{H} \rightarrow \mathbf{R}^{4 \times 4}$ is a matrix representing a left-quaternion matrix multiplication, and $\varphi : \mathbf{R}^3 \rightarrow \mathbf{H}$ is a mapping to a unit quaternion. The standard update (47) is used for the remaining decision variables b and c .

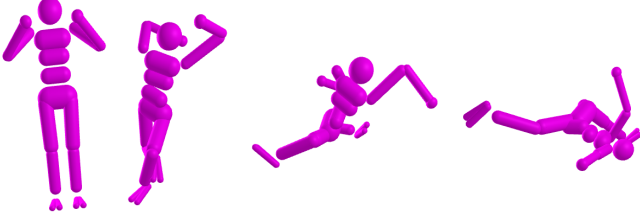


Fig. 6: Astronaut simulation for energy and momentum conservation test. Joints are initialized with zero velocities and randomly actuated for 1 second. The simulation is visualized, from left to right.

Violation metrics: Two metrics are used to measure progress: The constraint violation:

$$r_{\text{vio}} = \|r(w; \theta)\|_{\infty}, \quad (49)$$

and complementarity violation:

$$\kappa_{\text{vio}} = \max_i \{\|b^{(i)} \circ c^{(i)}\|_{\infty}\}. \quad (50)$$

The problem (27) is considered solved when $r_{\text{vio}} < r_{\text{tol}}$ and $\kappa_{\text{vio}} < \kappa_{\text{tol}}$.

Centering: The solver adaptively relaxes (27) by computing the centering parameters μ and σ . These values provide an estimate of the cone-constraint violation and determine the value of the central-path parameter that a correction step will aim to satisfy. These values rely on the degree of the cone [44]:

$$\mathbf{deg}(\mathcal{K}) = \sum_{i=1}^{n_{\mathcal{K}}} \mathbf{deg}(\mathcal{K}^{(i)}) = \mathbf{dim}(\mathcal{K}^{(1)}) + n_{\mathcal{K}} - 1, \quad (51)$$

the complementarity violations:

$$\mu = \frac{1}{\mathbf{deg}(\mathcal{K})} \sum_{i=1}^{n_{\mathcal{K}}} (b^{(i)})^T c^{(i)}. \quad (52)$$

and affine complementarity violations:

$$\mu^{\text{aff}} = \frac{1}{\mathbf{deg}(\mathcal{K})} \sum_{i=1}^{n_{\mathcal{K}}} (b^{(i)} + \alpha \Delta^{b^{(i)}})^T (c^{(i)} + \alpha \Delta^{c^{(i)}}), \quad (53)$$

as well as their ratio:

$$\sigma = \min \left(1, \max \left(0, \frac{\mu^{\text{aff}}}{\mu} \right) \right)^3, \quad (54)$$

As the algorithm makes progress, it aims to reduce these violations.

Algorithm: The interior-point algorithm used to solve (27) is summarized in Algorithm 2. Additional tolerances $\tau \in [0.9, 1]$ are used to improve numerical reliability of the solver. The algorithm parameters include $\tau_{\text{max}}^{\text{SOC}}$ to prevent the iterates from reaching the boundaries of the cones too rapidly during the solve, τ_{min} to ensure we are aiming at sufficiently large steps, and β is the decay rate of the step size α during the line search. In practice, r_{tol} and κ_{tol} are the only parameters the user might want to tune.

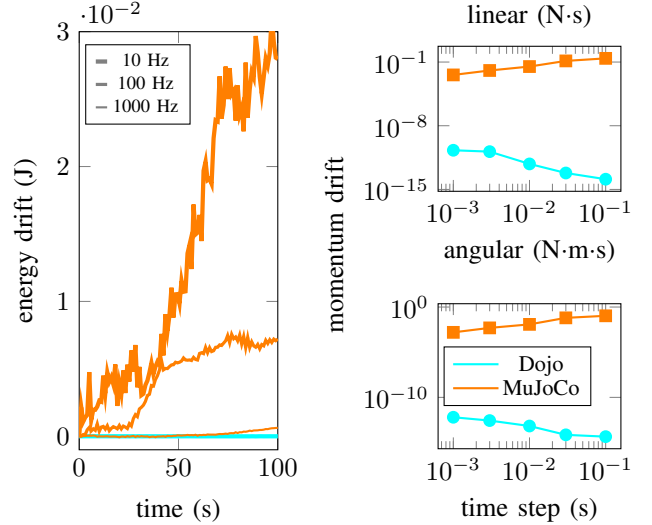


Fig. 7: Energy and momentum conservation comparison between MuJoCo and Dojo for the astronaut simulation (Fig 6) using time steps ranging from 0.001 to 0.1 second. Momentum drift is measured after actuating the astronaut for 1 second with random controls. Energy drift is measured over a 100 second simulation after 1 second of random actuation.

Finally, the algorithm outputs a solution $w^*(\theta, \kappa)$ that satisfies the solver tolerance levels and, optionally, the implicit gradients of the solution with respect to the problem parameters θ .

For an instance of problem (27), the algorithm is provided problem data and an initial point, which is projected to ensure that the cone variables are initially feasible with some margin. Next, an affine search direction (i.e., predictor) is computed that aims for zero complementarity violation. Using this direction, a cone line search is performed followed by a centering step that computes a target relaxation for the computation of the corrector search direction. A second cone line search is then performed for this new search direction. A subsequent line search is performed until either the constraint or complementarity violation is reduced. The current point is then updated, a new affine search direction is computed, and the procedure repeats until the violations satisfy the solver tolerances.

E. Gradients

Interior-point methods solve non-smooth problems by optimizing a sequence of smooth barrier sub-problems, where the degree of smoothing is parameterized by the central-path parameter κ . In the contact setting, we employ this same technique to return gradients that are informative through contact events. Intermediate solutions, $w^*(\theta, \kappa > 0)$, are differentiated using the implicit function theorem (11) to compute smooth *implicit gradients*. In practice, we find that these gradients greatly improve the performance of gradient-based optimization methods, consistent with the long history of interior-point methods. Dojo's gradients are compared with subgradients and randomized smoothing in Fig. 4. A wall-clock-time comparison of these gradients and sampled gradi-

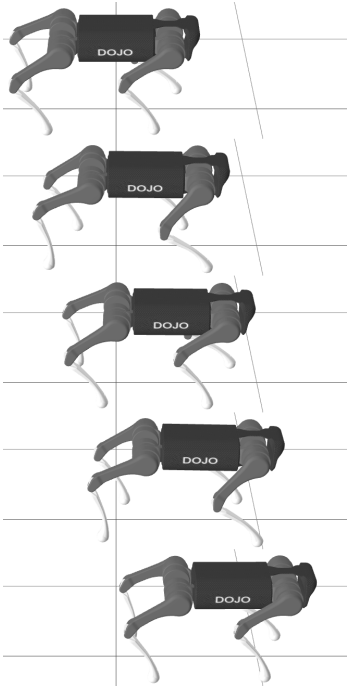


Fig. 8: Locomotion plan for quadruped generated using trajectory optimization. Time progresses top to bottom.

ents is provided in III, demonstrating that implicit gradients are more than an order of magnitude faster to compute.

The problem data for each simulation step include: the previous and current configurations, control input, and additional terms like the time step, friction coefficients, and parameters of each body.

F. Implementation

An open-source implementation, `Dojo.jl`, written in Julia, is available and a Python interface, `dojopy`, is also included. These tools, and the experiments, are available at:

<https://www.github.com/dojo-sim/Dojo.jl>.

V. RESULTS

Dojo’s capabilities are highlighted through a collection of examples, including: simulating physical phenomena, gradient-based planning with trajectory optimization, policy optimization, and system identification. The current implementation supports point, sphere, and capsule collisions with flat surfaces. All of the experiments were performed on a computer with an Intel Core i9-10885H processor and 32GB of memory.

A. Simulation

The simulation accuracy of Dojo and MuJoCo is compared in a number of illustrative scenarios.

Impact constraints comparison: The Atlas humanoid is simulated dropping onto a flat surface (Fig. 1). The system comprises 31 bodies, resulting in 403 maximal-coordinates states, and has 36 actuated degrees-of-freedom. Each foot has four contact points. A comparison with MuJoCo is performed

TABLE IV: Planning results. Comparison of final cost value, goal constraint violation, and total number of iterations for a collection of systems optimized with iterative LQR [24] using Dojo (D) with implicit gradients or MuJoCo (M) with finite-difference gradients.

System	Cost	Violation	Iterations
box right (D)	14.5	3e-3	30
box right (M)	13.5	3e-3	95
box up (D)	14.5	3e-3	106
box up (M)	failure	1.0	-
hopper (D)	8.9	1e-3	96
hopper (M)	26.7	2e-3	66
quadruped (D)	2e-2	3e-4	20

measuring penetration violations with the floor for different simulation rates (Table II). The current implementation of Dojo simulates this system in real time at 65 Hz. We expect this timing result to improve considerably with a more efficient implementation.

Friction-cone comparison: The effect of friction-cone approximation is demonstrated by simulating a box that is initialized with lateral velocity before impacting and sliding along a flat surface. The complementarity problem with P contact points requires $2P(1+2d)$ decision variables for contact and a corresponding number of constraints, where d is the degree of parameterization (e.g., double parameterization: $d = 2$). For a pyramidal approximation, in the probable scenario where its vertices are not aligned with the direction of motion, velocity drift occurs for a linearized cone implemented in Dojo and MuJoCo (Fig. 5). While it is possible to reduce such artifacts by increasing the number of vertices in the approximation of the second-order cone, this increases the computational complexity. Such approximation is unnecessary in Dojo as we handle the exact nonlinear cone constraint efficiently and reliably with optimization tools from cone programming; the result is accurate sliding.

Energy and momentum conservation: An accurate physics engine conserves important physical quantities like energy and momentum. Following the methodology from [12], we simulate “astronaut,” a free-floating humanoid, and measure the drift of these quantities (Fig. 7). There is no internal damping or springs, joint limits, or contact, and gravity is turned off. The astronaut is initialized with no linear or angular velocity and momentum drift is computed after one second of uniformly sampled actuation: $u \sim \mathcal{U}(0, 0.05)$. Energy drift is computed over a 100 second period after 1 second of random actuation. MuJoCo exhibits drift in all scenarios. Characteristic of its variational integrator, Dojo conserves both linear and angular momentum to machine precision. Energy does not drift for Dojo but exhibits small bounded oscillations that decrease in amplitude as the time step decreases (Fig. 7). Conservation of energy to machine precision with variational integrators is possible and is a topic of current research [37].

B. Planning

Iterative LQR utilizes implicit gradients [16] from Dojo to perform trajectory optimization on three systems: planar box, hopper, and quadruped. A comparison is performed with MuJoCo and finite-difference gradients. The results are

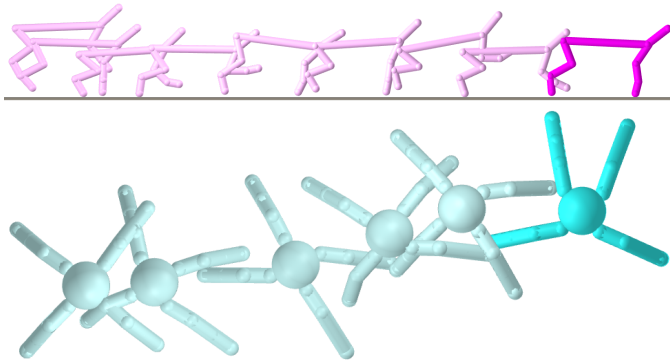


Fig. 9: Learned policy rollouts for half-cheetah (top) and ant (bottom). Time progresses left to right.

visualized for the quadruped in Fig. 8 and summarized for all of the systems in Table IV.

Box: Inputs are optimized to move a stationary rigid body that is resting on a flat surface (Fig. 4) to a goal location that is either to the right or up in the air 1 meter. The planning horizon is 1 second and the controls are initialized with zeros. Dojo uses a time step $h = 0.1$, whereas MuJoCo uses $h = 0.01$ to prevent significant contact violations with the floor. MuJoCo fails in the scenario with the goal in the air, while Dojo succeeds at both tasks.

Hopper: The hopping robot [36] with $m = 3$ controls and $n = 14$ degrees-of-freedom is tasked with moving to a target pose over 1 second. Similar, although not identical, models and costs are used. Dojo uses a time step $h = 0.05$ whereas MuJoCo uses $h = 0.01$. The hopper is initialized with controls that maintain its standing configuration. Quadratic costs are used to penalize control effort and perform cost shaping on an intermediate state in the air and the goal pose. The optimizer typically finds a single-hop motion.

Quadruped: The Unitree A1 with $m = 12$ controls and $n = 36$ degrees-of-freedom is tasked with moving to a goal location over a planning horizon $T = 41$ with time step $h = 0.05$. Controls are initialized to compensate for gravity and there are costs on tracking a target kinematic gait and control inputs. The optimizer finds a dynamically feasible motion that closely tracks the kinematic plan.

Overall, we find that final results from both engines are similar. However, importantly, MuJoCo is enforcing soft contact whereas Dojo simulates hard contact. Dojo’s gradients are computed with $\kappa = 3e-4$. Further, for systems with contact, MuJoCo requires a time step $h = 0.01$ for successful optimization, whereas Dojo succeeds with $h = 0.05$.

C. Policy Optimization

Gym-like environments [4, 10]: ant and half-cheetah are implemented in Dojo and we train static linear policies for locomotion. As a baseline, we employ Augmented Random Search (ARS) [28], a gradient-free approach coupling random search with a number of simple heuristics. For comparison, we train the same policies using augmented gradient search (AGS) which replaces the stochastic-gradient estimation of ARS with

TABLE V: Policy optimization results. Comparison of total reward, number of simulation-step and gradient evaluations for a collection of policies trained with Augmented Random Search (ARS) [28] and Augmented Gradient Search (AGS). The results are averaged over the best 3 out of 5 runs with different random seeds. Optimizing with gradients reaches similar performance levels while being 5 to 10 times more sample efficient.

System	Reward	Simulation Evals	Gradient Evals
half-cheetah (ARS)	46 ± 24	3e+4	0
ant (ARS)	64 ± 15	2e+5	0
half-cheetah (AGS)	44 ± 24	5e+3	5e+3
ant (AGS)	54 ± 28	2e+4	2e+4

Dojo’s implicit gradients. Policy rollouts are visualized in Fig. 9 and results are summarized in Table V.

Half-cheetah: This planar system with $m = 6$ controls and $n = 18$ degrees-of-freedom is rewarded for forward velocity and penalized for control effort over a horizon $T = 80$ with time step $h = 0.05$.

Ant: The system has $m = 8$ controls and $n = 28$ degrees-of-freedom and is rewarded for forward motion and maintaining a certain altitude and is penalized for control effort and contact over a horizon $T = 150$ with time step $h = 0.05$.

First, we are able to successfully train policies using this simple learning algorithm in Dojo’s hard contact environments. Second, MuJoCo requires smaller $h = 0.01$ time steps for stable simulation, whereas Dojo is stable with $h = 0.05$. Third, our initial results indicate that it is possible to train comparable policies in Dojo with 5 to 10 times less samples by utilizing implicit gradients compared to the gradient-free method.

D. System Identification

System identification is performed on an existing real-world dataset of trajectories collected by throwing a box on a table with different initial conditions [35]. We learn a set of parameters $\theta = (c_f, p^{(1)}, \dots, p^{(8)})$ that include the friction coefficient c_f , and 3-dimensional vectors $p^{(i)}$ that represent the position of vertex i of the box with respect to its center of mass.

Each trajectory is decomposed into $T - 2$ triplets of consecutive configurations: $Z = (z_-, z, z_+)$, where T is the number of time steps in the trajectory. Using the initial conditions z_-, z from a tuple, and an estimate of the system’s parameters θ , Dojo performs one-step simulation to predict the next state, \hat{z}_+ . Implicit gradients are utilized by a Gauss-Newton method to perform gradient-based learning of the system parameters.

The parameters are learned by minimizing the following loss:

$$\mathcal{L}(\mathcal{D}, \theta) = \sum_{Z \in \mathcal{D}} L(Z, \theta) = \sum_{Z \in \mathcal{D}} \frac{1}{2} \|\text{Dojo}(z_-, z; \theta) - z_+\|_W^2, \quad (55)$$

where $\|\cdot\|_W$ is a weighted norm, which aims to minimize the difference between the ground-truth trajectories and physics-engine predictions. We use gradients:

$$\frac{\partial L}{\partial \theta} = \frac{\partial \text{Dojo}}{\partial \theta}^T W (\text{Dojo}(z_-, z; \theta) - z_+), \quad (56)$$

and approximate Hessians:

$$\frac{\partial^2 L}{\partial \theta^2} \approx \frac{\partial \mathbf{Dojo}^T}{\partial \theta} W \frac{\partial \mathbf{Dojo}}{\partial \theta}. \quad (57)$$

Gradients are computed with $\kappa = 3e-4$.

After training, the learned parameters are within 5% of the true geometry and best-fit friction coefficient for the box from the dataset. We complete the real-to-sim transfer and simulate the learned system in Dojo, comparing it to the ground-truth dataset trajectories. Results are visualized in Fig. 10.

VI. CONCLUSION

Dojo is designed from physics- and optimization-first principles to enable better gradient-based optimization for planning, control, policy optimization, and system identification.

A. Contributions

The engine makes several advancements over previous state-of-the-art engines for robotics: First, the variational integrator enables stable simulation at low sample rates. Second, the contact model includes an improved friction model that eliminates artifacts like creep, particularly for sliding, and hard contact for impact is achieved to machine precision. This should enable superior sim-to-real transfer for both locomotion and manipulation applications. The underlying interior-point solver, developed specifically for solving NCPs, is numerically robust and requires practically no hyperparameter tuning for good performance across numerous systems, and handles cone and quaternion variables. Third, the engine efficiently returns implicit gradients that are smooth and analytical, providing useful information through contact events. Fourth, in addition to building and providing an open-source tool, the physics and optimization algorithms presented can improve many existing engines.

B. Limitations

In terms of features, reliability, and wall-clock time, MuJoCo—the product of a decade of excellent software engineering—is impressive. As development of Dojo continues, we expect to make significant progress in all of these areas. However, fundamentally, Dojo’s approach of solving an NCP with a primal-dual interior-point method will likely be computationally more expensive compared to MuJoCo’s convex soft-contact model, which can never entirely recover accurate solutions even at higher sampling frequencies. This is the fundamental trade-off Dojo makes for robotics applications: greater computational cost for accurate physics and smooth gradients.

Additionally, because Dojo solves a nonlinear complementarity problem (i.e, non-convex problem) at each time step the engine provides no guarantees of converging to a solution. In practice, we do not find this to be a problem, but for time- or safety-critical applications this should be a consideration. Further, it remains to be seen how well sim-to-real transfer works, in comparison to existing engines, particularly for manipulation tasks with a large number of contact interactions.

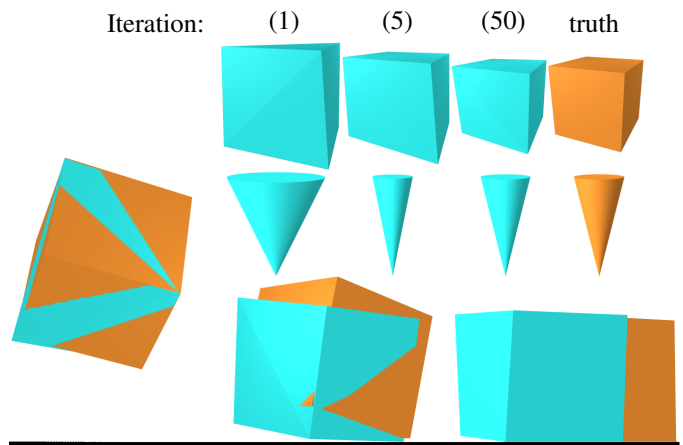


Fig. 10: System identification. Top right: Learning box geometry and friction cone to less than 5% error. Bottom: Simulated trajectory of the box using the learned properties (blue) compared to ground truth (orange).

C. Future Work

A number of future improvements to Dojo are planned. First, Dojo currently implements simple collision detection (e.g., sphere-halfspace, sphere-sphere). Natural extensions include support for convex primitives and curved surfaces. Another improvement is adaptive time stepping. Similar to advanced numerical integrators for stiff systems, Dojo should take large time steps when possible and adaptively modify the time step in cases of numerical difficulties or physical inaccuracies. Finally, hardware-accelerator support for Dojo would potentially enable faster simulation and optimization.

Perhaps the most important remaining question is whether the physics and optimization improvements from this work translate into better transfer of simulation results to successes on real-world robotic hardware. In this thrust, future work will explore the transfer of control policies trained in Dojo to hardware and deployment of the engine in model predictive control frameworks.

In conclusion, we have presented a new physics engine, Dojo, specifically designed for robotics. This tool is the culmination of a number of improvements to the contact dynamics model and underlying optimization routines, aiming to advance state-of-the-art physics engines for robotics by improving physical accuracy and differentiability.

ACKNOWLEDGEMENTS

The authors would like to thank Suvansh Sanjeev for assistance with the Python interface. Toyota Research Institute provided funds to support this work.

REFERENCES

- [1] Ilge Akkaya, Marcin Andrychowicz, Maciek Chociej, Mateusz Litwin, Bob McGrew, Arthur Petron, Alex Paino, Matthias Plappert, Glenn Powell, Raphael Ribas, et al. Solving Rubik’s cube with a robot hand. *arXiv:1910.07113*, 2019.

- [2] OpenAI: Marcin Andrychowicz, Bowen Baker, Maciek Chociej, Rafal Jozefowicz, Bob McGrew, Jakub Pachocki, Arthur Petron, Matthias Plappert, Glenn Powell, Alex Ray, et al. Learning dexterous in-hand manipulation. *The International Journal of Robotics Research*, 39(1):3–20, 2020.
- [3] Stephen Boyd and Lieven Vandenbergh. *Convex Optimization*. Cambridge University Press, 2004.
- [4] Greg Brockman, Vicki Cheung, Ludwig Pettersson, Jonas Schneider, John Schulman, Jie Tang, and Wojciech Zaremba. OpenAI Gym. *arXiv:1606.01540*, 2016.
- [5] Jan Brüdigam and Zachary Manchester. Linear-time variational integrators in maximal coordinates. In *International Workshop on the Algorithmic Foundations of Robotics*, pages 194–209, 2020.
- [6] Jan Brüdigam, Jana Janeva, Stefan Sosnowski, and Sandra Hirche. Linear-time contact and friction dynamics in maximal coordinates using variational integrators. *arXiv:2109.07262*, 2021.
- [7] Richard W. Cottle, Jong-Shi Pang, and Richard E. Stone. *The Linear Complementarity Problem*. SIAM, 2009.
- [8] Erwin Coumans and Yunfei Bai. PyBullet, a Python module for physics simulation for games, robotics and machine learning, 2016–2019. URL <http://pybullet.org>.
- [9] Ulisse Dini. *Lezioni di analisi infinitesimale*, volume 1. Fratelli Nistri, 1907.
- [10] Yan Duan, Xi Chen, Rein Houthoofd, John Schulman, and Pieter Abbeel. Benchmarking deep reinforcement learning for continuous control. In *International Conference on Machine Learning*, pages 1329–1338, 2016.
- [11] Ryan Elandt, Evan Drumwright, Michael Sherman, and Andy Ruina. A pressure field model for fast, robust approximation of net contact force and moment between nominally rigid objects. In *IEEE/RSJ International Conference on Intelligent Robots and Systems*, pages 8238–8245, 2019.
- [12] Tom Erez, Yuval Tassa, and Emanuel Todorov. Simulation tools for model-based robotics: Comparison of Bullet, Havok, MuJoCo, ODE and PhysX. In *IEEE International Conference on Robotics and Automation*, pages 4397–4404, 2015.
- [13] C. Daniel Freeman, Erik Frey, Anton Raichuk, Sertan Girgin, Igor Mordatch, and Olivier Bachem. Brax—A differentiable physics engine for large scale rigid body simulation. *arXiv:2106.13281*, 2021.
- [14] Moritz Geilinger, David Hahn, Jonas Zehnder, Moritz Bächer, Bernhard Thomaszewski, and Stelian Coros. ADD: Analytically differentiable dynamics for multi-body systems with frictional contact. *ACM Transactions on Graphics*, 39(6):1–15, 2020.
- [15] Eric Heiden, David Millard, Erwin Coumans, Yizhou Sheng, and Gaurav S. Sukhatme. NeuralSim: Augmenting differentiable simulators with neural networks. *IEEE International Conference on Robotics and Automation*, pages 9474–9481, 2021.
- [16] Taylor A. Howell, Simon Le Cleac’h, Sumeet Singh, Pete Florence, Zachary Manchester, and Vikas Sindhwani. Trajectory optimization with optimization-based dynamics. *IEEE Robotics and Automation Letters*, 7(3):6750–6757, 2022.
- [17] Yuanming Hu, Luke Anderson, Tzu-Mao Li, Qi Sun, Nathan Carr, Jonathan Ragan-Kelley, and Frédo Durand. DiffTaichi: Differentiable programming for physical simulation. *International Conference on Learning Representations*, 2020.
- [18] Brian E. Jackson, Kevin Tracy, and Zachary Manchester. Planning with attitude. *IEEE Robotics and Automation Letters*, 6(3):5658–5664, 2021.
- [19] Nathan Koenig and Andrew Howard. Design and use paradigms for Gazebo, an open-source multi-robot simulator. In *IEEE/RSJ International Conference on Intelligent Robots and Systems*, volume 3, pages 2149–2154, 2004.
- [20] Ashish Kumar, Zipeng Fu, Deepak Pathak, and Jitendra Malik. RMA: Rapid motor adaptation for legged robots. *arXiv:2107.04034*, 2021.
- [21] Jeongseok Lee, Michael X. Grey, Sehoon Ha, Tobias Kunz, Sumit Jain, Yuting Ye, Siddhartha S. Srinivasa, Mike Stilman, and C. Karen Liu. DART: Dynamic animation and robotics toolkit. *Journal of Open Source Software*, 3(22):500, 2018.
- [22] Joonho Lee, Jemin Hwangbo, Lorenz Wellhausen, Vladlen Koltun, and Marco Hutter. Learning quadrupedal locomotion over challenging terrain. *Science Robotics*, 5(47), 2020.
- [23] Sergey Levine, Peter Pastor, Alex Krizhevsky, Julian Ibarz, and Deirdre Quillen. Learning hand-eye coordination for robotic grasping with deep learning and large-scale data collection. *The International Journal of Robotics Research*, 37(4-5):421–436, 2018.
- [24] Weiwei Li and Emanuel Todorov. Iterative linear quadratic regulator design for nonlinear biological movement systems. In *International Conference on Informatics in Control, Automation and Robotics*, pages 222–229, 2004.
- [25] Miguel Sousa Lobo, Lieven Vandenbergh, Stephen Boyd, and Hervé Lebret. Applications of second-order cone programming. *Linear Algebra and its Applications*, 284(1-3):193–228, 1998.
- [26] Zachary Manchester and Scott Kuindersma. Variational contact-implicit trajectory optimization. In *Robotics Research*, pages 985–1000. Springer, 2020.
- [27] Zachary R. Manchester and Mason A. Peck. Quaternion variational integrators for spacecraft dynamics. *Journal of Guidance, Control, and Dynamics*, 39(1):69–76, 2016.
- [28] Horia Mania, Aurelia Guy, and Benjamin Recht. Simple random search of static linear policies is competitive for reinforcement learning. In *Advances in Neural Information Processing Systems*, pages 1800–1809, 2018.
- [29] Jerrold E. Marsden and Matthew West. Discrete mechanics and variational integrators. *Acta Numerica*, 10: 357–514, 2001.
- [30] Sanjay Mehrotra. On the implementation of a primal-dual interior point method. *SIAM Journal on Optimization*, 2(4):575–601, 1992.
- [31] Jean Jacques Moreau. On unilateral constraints, friction

- and plasticity. In *New Variational Techniques in Mathematical Physics*, pages 171–322. Springer, 2011.
- [32] Jorge Nocedal and Stephen J. Wright. *Numerical Optimization*. Springer, second edition, 2006.
- [33] Nvidia. PhysX physics engine, 2022. URL <https://developer.nvidia.com/physx-sdk>.
- [34] Mihir Parmar, Mathew Halm, and Michael Posa. Fundamental challenges in deep learning for stiff contact dynamics. In *2021 IEEE/RSJ International Conference on Intelligent Robots and Systems (IROS)*, pages 5181–5188, 2021. doi: 10.1109/IROS51168.2021.9636383.
- [35] Samuel Pfrommer, Mathew Halm, and Michael Posa. ContactNets: Learning discontinuous contact dynamics with smooth, implicit representations. In *Conference on Robot Learning*, pages 2279–2291, 2021.
- [36] Marc H. Raibert, H. Benjamin Brown Jr., Michael Chepponis, Jeff Koechling, Jessica K. Hodgins, Diane Dustman, W. Kevin Brennan, David S. Barrett, Clay M. Thompson, John Daniell Hebert, Woojin Lee, and Borvansky Lance. Dynamically stable legged locomotion. Technical report, Massachusetts Institute of Technology Cambridge Artificial Intelligence Lab, 1989.
- [37] Harsh Sharma, Mayuresh Patil, and Craig Woolsey. Energy-preserving variational integrators for forced Lagrangian systems. *Communications in Nonlinear Science and Numerical Simulation*, 64:159–177, 2018.
- [38] David E. Stewart and Jeffrey C. Trinkle. An implicit time-stepping scheme for rigid body dynamics with inelastic collisions and Coulomb friction. *International Journal for Numerical Methods in Engineering*, 39(15): 2673–2691, 1996.
- [39] Hyung Ju Terry Suh, Tao Pang, and Russ Tedrake. Bundled gradients through contact via randomized smoothing. *IEEE Robotics and Automation Letters*, 7(2):4000–4007, 2022.
- [40] Yuval Tassa, Tom Erez, and Emanuel Todorov. Synthesis and stabilization of complex behaviors through online trajectory optimization. In *IEEE/RSJ International Conference on Intelligent Robots and Systems*, pages 4906–4913, 2012.
- [41] Russ Tedrake and the Drake Development Team. Drake: Model-based design and verification for robotics, 2019. URL <https://drake.mit.edu>.
- [42] Emanuel Todorov. Convex and analytically-invertible dynamics with contacts and constraints: Theory and implementation in MuJoCo. In *IEEE International Conference on Robotics and Automation*, pages 6054–6061, 2014.
- [43] Emanuel Todorov, Tom Erez, and Yuval Tassa. MuJoCo: A physics engine for model-based control. In *IEEE/RSJ International Conference on Intelligent Robots and Systems*, pages 5026–5033, 2012.
- [44] Lieven Vandenbergh. The CVXOPT linear and quadratic cone program solvers. *Online: <http://cvxopt.org/documentation/coneprog.pdf>*, 2010.
- [45] Keenon Werling, Dalton Omens, Jeongseok Lee, Ioannis Exarchos, and C. Karen Liu. Fast and feature-complete differentiable physics for articulated rigid bodies with contact. *arXiv:2103.16021*, 2021.
- [46] Wenshuai Zhao, Jorge Peña Queraltá, and Tomi Westerlund. Sim-to-real transfer in deep reinforcement learning for robotics: a survey. In *2020 IEEE Symposium Series on Computational Intelligence (SSCI)*, pages 737–744, 2020. doi: 10.1109/SSCI47803.2020.9308468.

APPENDIX A QUATERNION ALGEBRA

In this section we introduce a set of conventions for notating standard quaternion operations, adopted from [5, 18], and employed in the rotational part of our variational integrator (17).

Quaternions are written as four-dimensional vectors:

$$q = (s, v) = (s, v_1, v_2, v_3) \in \mathbf{H}, \quad (58)$$

where s and v are scalar and vector components, respectively. Dojo employs unit quaternions (i.e., $q^T q = 1$) to represent orientation, providing a mapping from the local body frame to a global inertial frame.

Quaternion multiplication is represented using linear algebra (i.e., matrix-vector and matrix-matrix products). Left and right quaternion multiplication:

$$q^a \cdot q^b = \begin{bmatrix} s^a s^b - (v^a)^T v^b \\ s^a v^b + s^b v^a + v^a \times v^b \end{bmatrix} = L(q^a)q^b = R(q^b)q^a, \quad (59)$$

where \times is the standard vector cross product, is represented using the matrices:

$$L(q) = \begin{bmatrix} s & -v^T \\ v & sI_3 + \mathbf{skew}(v) \end{bmatrix} \in \mathbf{R}^{4 \times 4}, \quad (60)$$

$$R(q) = \begin{bmatrix} s & -v^T \\ v & sI_3 - \mathbf{skew}(v) \end{bmatrix} \in \mathbf{R}^{4 \times 4}, \quad (61)$$

where:

$$\mathbf{skew}(x) = \begin{bmatrix} 0 & -x_3 & x_2 \\ x_3 & 0 & -x_1 \\ -x_2 & x_1 & 0 \end{bmatrix}, \quad (62)$$

is defined such that:

$$\mathbf{skew}(x)y = x \times y, \quad (63)$$

and I_3 is a 3-dimensional identity matrix. The vector component of a quaternion:

$$v = Vq, \quad (64)$$

is extracted using the matrix:

$$V = [\mathbf{0} \quad I_3] \in \mathbf{R}^{3 \times 4}, \quad (65)$$

and quaternion conjugate:

$$q^\dagger = \begin{bmatrix} s \\ -v \end{bmatrix} = Tq, \quad (66)$$

is computed using:

$$T = \begin{bmatrix} 1 & \mathbf{0}^T \\ \mathbf{0} & -I_3 \end{bmatrix} \in \mathbf{R}^{4 \times 4}. \quad (67)$$